Nuclear Engineering and Technology xxx (xxxx) xxx

Contents lists available at ScienceDirect

Nuclear Engineering and Technology

journal homepage: www.elsevier.com/locate/net

Original Article

Waste to shield: Tailoring cordierite/mullite/zircon composites for radiation protection through controlled sintering and Y_2O_3 addition

Celal Avcıoğlu [a,b,c,*], Recep Artır [a]

[a] Marmara University, Faculty of Engineering, Department of Metallurgical and Materials Engineering, 34854, Istanbul, Turkey
[b] Technische Universität Berlin, Faculty III Process Sciences, Institute of Material Science and Technology, Fachgebiet Keramische Werkstoffe / Chair of Advanced Ceramic Materials, Straße des 17. Juni 135, 10623, Berlin, Germany
[c] Scientific Research Projects Coordinatorship, Usak University, 64000, Usak, Turkey

ARTICLE INFO

Keywords:
Investment casting shell waste
Ceramic recycling
Cordierite-mullite composite
Gamma-ray attenuation
Neutron shielding
Y_2O_3 additive

ABSTRACT

In this study, investment casting shell waste successfully utilized to produce cordierite/mullite/zircon composites. Green pellets, consisting of investment casting shell waste, alumina, and magnesia, were prepared and sintered at temperatures between 1250 and 1350 °C. The influence of the sintering temperature on the crystalline phase composition, densification behavior, flexural strength, microstructure, and radiation shielding properties of the cordierite/mullite/zircon composites is investigated. Phase analysis showed that characteristic cordierite peaks appear at 1250 °C, but the complete conversation of silica from investment casting shell waste into cordierite requires a sintering temperature of at least 1300 °C. Notably, the cordierite/mullite/zircon composite sintered at 1350 °C exhibited a sixfold increase in flexural strength compared to the ceramic composite directly fabricated from investment casting shell waste at the same sintering temperature. Furthermore, the effect of Y_2O_3 addition on composites' radiation shielding properties is investigated. The results show that the Y_2O_3 addition improves densification behavior, enhancing the shielding capabilities of the composites against fast neutron and gamma radiation. Our findings suggest that the developed ceramic composites show significant potential for gamma-ray and neutron shielding applications.

1. Introduction

Radiation shielding has emerged as a critical consideration in various industries, including nuclear energy, healthcare, aerospace, and space exploration. Safeguarding human health and sensitive equipment from the adverse effects of ionizing radiation is paramount. However, conventional radiation shielding materials, like lead and concrete, face durability issues when subjected to elevated temperatures. This challenge is particularly significant in the context of nuclear reactor cores, where temperatures can reach 1000 °C [1]. To address these limitations, researchers explore alternative materials, including advanced ceramics, refractory metals, and specialized high-temperature alloys, to ensure reliable and durable radiation shielding in the demanding conditions of nuclear reactor environments [2–26].

Cordierite ($Mg_2Al_4Si_5O_{18}$) is a well-established structural ceramic material within the $MgO–Al_2O_3–SiO_2$ ternary system. Renowned for its excellent thermal shock resistance, chemical durability, low thermal expansion coefficient ($0.7*10^{-6}$ K^{-1}, 25–1000 °C), and dielectric permittivity ($\varepsilon r \approx 4$ at 1 MHz) [27–29], cordierite ceramics are commonly employed as refractories, catalytic converters, electro-ceramics, membranes, and tableware [30,31].

Nevertheless, despite its wide use, cordierite rarely occurs in nature. Therefore, most cordierite ceramics used in the industry are produced synthetically. Among various methods, reaction sintering proved to be the most economical way for industrial-scale cordierite production. Natural raw materials containing oxides of MgO, Al_2O_3, and SiO_2 are often employed as raw materials for cordierite production. Commonly used raw materials include clay, talc, kaolin, alumina, silica sand, feldspar, and quartz [32,33]. However, to reduce the cost of cordierite ceramics, researchers have explored the potential of various industrial wastes, including waste magnesite powder, serpentine waste, kiln rollers waste, kaolin waste, fly ash, aluminum slag, and aluminum sludge as alternative raw materials [34–37].

Investment casting shell moulds, comprising silica, zircon, alumina, and aluminum silicates like mullite, are valuable refractory materials widely used in the investment casting process. Despite their high

---

[*] Corresponding author. Marmara University, Faculty of Engineering, Department of Metallurgical and Materials Engineering, 34854, Istanbul, Turkey.
E-mail address: celal.avcioglu@usak.edu.tr (C. Avcıoğlu).

https://doi.org/10.1016/j.net.2024.02.038
Received 5 November 2023; Received in revised form 22 January 2024; Accepted 19 February 2024

Please cite this article as: Celal Avcıoğlu, Recep Artır, *Nuclear Engineering and Technology*, https://doi.org/10.1016/j.net.2024.02.038

Table 1
Chemical composition (wt.%) of W powder using XRF [39].

Al	Si	Ca	Ti	Fe	Sr	Zr	Nb	Na	P	K	O
14.78	24.79	0.14	1.85	0.45	0.05	12.33	0.02	0.04	0.03	0.16	45.77

production costs and excellent refractory properties, these shell moulds are often discarded after casting, resulting in substantial waste. The inability to recycle investment casting shell waste (ICSW) in the casting industry underscores the need for alternative methods to repurpose this waste and mitigate its environmental impact.

In response to this challenge, we propose an innovative approach to utilize ICSW as a raw material in the production of cordierite-mullite-zircon composites. Cordierite ceramics, renowned for their outstanding refractory properties, are well-suited for harsh radiation environments encountered in the nuclear industry. However, their inherent porosity can impact their radiation shielding ability. To address this limitation, Y_2O_3 introduced as an additive, leveraging its known capability to enhance densification and mechanical properties of mullite and cordierite-based ceramics through liquid phase sintering [38–40]. Additionally, the higher atomic weight of Y compared to Al, Si, and Mg may contribute to improved gamma ray attenuation capabilities due to its higher proton count and greater electron density in inner electron shells, advantageous for the photoelectric absorption process [38].

Our study focuses on the cost-effective fabrication of cordierite/mullite/zircon composites by sintering a mixture of ICSW, alumina, and magnesia at various temperatures. The detailed investigation encompasses the impact of sintering temperature and Y_2O_3 addition on key properties of the composites, including crystal phase composition, morphology, bulk density, apparent porosity, and flexural strength.

While previous research has explored the refractory properties of cordierite-mullite composites [41], our study distinguishes itself by incorporating recycled materials in their synthesis and specifically examining their radiation shielding capabilities.

2. Materials and methods

The ICSW was obtained from a foundry plant in Istanbul-Turkey. Detailed characterization data for the waste material and the pre-treatment process have been previously published [39]. In summary, the waste was processed by grinding large chunks into a fine powder, which was then screened through a 63 μm sieve to create a feedstock. The crystal phase composition of the investment casting shell waste powder includes zircon, quartz, cristobalite, mullite, and corundum and its chemical composition determined by XRF analysis is given in Table 1.

Cordierite-based composites prepared as follows. The batch formulation included ICSW, alumina, and magnesia, with the goal of converting all free silica in the waste into cordierite, as indicated by the XRF results and the following equation:

$$2Al_2O_3\ (s) + 2MgO\ (s) + 5SiO_2\ (s) \rightarrow Mg_2Al_4Si_5O_{18}\ (s) \qquad \text{(eq.1)}$$

The determined batch composition contains ICSW, alumina, and magnesia in a 100: 17.7: 9.8 wt ratio. Additionally, several batches were prepared by adding 1 to 10 wt% of Y_2O_3 to the base composition. Furthermore, for comparison, ceramic composites from ICSW without any additives were also prepared.

The raw materials were accurately weighed and thoroughly mixed using a planetary ball mill for 2 h in an alumina jar with high-purity alumina grinding media and water. The resulting mixture was dried overnight at 80 °C, followed by crushing in an agate mortar with a pestle. Rectangular green bodies (50 mm × 20 mm x 8 mm) were fabricated through uni-axial pressing at a pressure of 200 MPa.1 wt %—polyvinyl alcohol and stearic acid were used as a binder and internal lubricant, respectively for the preparation of green bodies. Thermal debinding was conducted at 500 °C for 2 h with a heating rate of 2 °C/min in an electrical furnace. Subsequently, the green bodies were sintered at 1250 °C, 1300 °C, or 1350 °C for 3 h with heating and cooling rates of 5 °C/min. Sample codes, batch compositions, and sintering temperatures are listed in Table 2.

Crystalline phase compositions of samples analyzed by X-ray powder diffraction technique with a D8 Advance X-ray diffractometer (Bruker, Germany) by CuKα radiation ($\lambda = 1.5406$ Å). Measurements were taken in the 2θ range of 8–80° with a step size of 0.1° and time intervals of 8s. The elemental composition of the ICSW was analyzed using an X-ray fluorescence spectrometer (Rigaku, Japan). The XRF analysis was conducted under an air atmosphere, and a 10 mm collimator was used. The three-point bending test was conducted from bar (20 mm × 8 mm x 8 mm) shaped samples. Samples were gently polished before experiments, and a crosshead speed of 0.5 mm/min was applied. Five replicas of each sample were tested, and their average values were obtained. The microstructural analysis was performed from fractured surfaces of samples upon a 3-point bending test using scanning electron microscopy (Quanta Feg 250, FEI, USA). The bulk density and apparent porosity of sintered ceramic composites were determined by the Archimedes method, based on the ASTM C-373-18. Initially, dry weights ($\mathbf{W_d}$) of samples were measured before Archimedes' experiment. Afterward, samples were boiled in water at 120 °C for 4 h until the open porosity was filled with water. Then, their suspended weights ($\mathbf{W_s}$) were measured while they were in the water. Lastly, they were removed from the water, and their surface water was cleaned gently with paper towels before being weighed to determine their saturated weights ($\mathbf{W_m}$).

The bulk density (ρ) of samples was determined by the following equation;

$$\rho = \frac{W_d}{W_m - W_s}$$

The apparent porosity (φ) of samples was determined by the following equation;

$$\varphi = \frac{W_m - W_d}{W_m - W_s}$$

Linear shrinkage of samples was measured by measuring the largest side of the rectangular (50 mm × 20 mm x 8 mm) ceramic bodies before and after sintering using a digital micrometer. Then the linear shrinkage was determined as follows;

$$\text{Linear shrinkage } (\%) = \frac{d_0 - d_f}{d_0}\ 100$$

Table 2
Sample codes and batch compositions. ("ICSW" represents investment casting shell waste).

Sample	Sintering Temperature (°C)	Composition (wt.%)			
		ICSW	Al_2O_3	MgO	Y_2O_3
W-1250	1250	100	–	–	–
W-1300	1300	100	–	–	–
W-1350	1350	100	–	–	–
MAW-1250	1250	78.4	13.9	7.7	–
MAW-1300	1300	78.4	13.9	7.7	–
MAW-1350	1350	78.4	13.9	7.7	–
MAW-1350- Y1	1350	77.7	13.7	7.6	1
MAW-1350- Y3	1350	76.1	13.5	7.5	2.9
MAW-1350- Y5	1350	74.7	13.2	7.3	4.8
MAW-1350- Y7	1350	73.3	13	7.2	6.5
MAW-1350- Y10	1350	71.3	12.6	7	9.1

d_0 *and* d_f are the diameters of samples before and after sintering.

The linear mass attenuation coefficient of the ceramic composites was determined using the gamma-ray shielding experimental setup. The details of the gamma-ray shielding experimental setup were recently published elsewhere [40–42]. Briefly, the setup contains a NaI(Tl) scintillation detector with a 3 × 3 inches diameter and a photomultiplier tube. The resolution of the NaI(Tl) crystal is approximately 7% at a photon energy of 662 keV for ^{137}Cs, and the light decay time constant is approximately 0.23 μs Experiments were carried out from disc-shaped samples with 1.2 cm diameter and varying thicknesses from 0.5318 to 0.627. The linear mass attenuation coefficients of the samples were determined for two energy lines for ^{133}Ba (81 keV and 356 keV) and another one for the 137Cs (662 keV) source. Each measurement was performed three times for 20 min, and their average values were obtained. The statistical error was lower than 2%. Furthermore, the PhyX/PSD program was used to explore the radiation shielding ability of manufactured ceramics theoretically [43,44].

3. Results and discussion

The XRD analysis of the ICSW powder reveals that it is mainly composed of zircon, quartz, cristobalite, mullite, and corundum phases, as shown in Fig. 1. It is now well-established that quartz transforms into cristobalite at elevated temperatures. From 1250 to 1350 °C, the peak intensity of quartz indeed decreases where almost no quartz was detected for the W-1350 sample. However, the peak intensity of cristobalite, along with that of corundum, also declined with increasing sintering temperature. Meanwhile, the relative intensity of mullite peaks slightly increases. This observation is probably due to the mullite formation reaction between silica and alumina, which starts at about 1250 °C and accelerates with increasing firing temperature. Nevertheless, both corundum and cristobalite phases are still evident for W-1350. This indicates that firing ICSW at 1350 °C for 4 h is not sufficient to complete the mullite formation reaction.

Fig. 2 shows the XRD patterns of the fired pellets prepared from alumina, magnesia, and ICSW powder mixture to obtain cordierite-containing composites at 1250–1350 °C for 3 h. The formation of cordierite was first observed at 1250 °C. This might be attributed to the reaction among corundum, magnesia, and silica, based on Equation (1). Nonetheless, the fraction of formed cordierite at 1250 °C was low. Besides, a large amount of cristobalite and corundum phases are still present. As temperature increases, the corresponding cordierite peaks become stronger and narrower. Meanwhile, cristobalite disappears first and then almost corundum. Thereby, ceramic composites mainly composed of cordierite, mullite, and zircon are obtained for the MAW-1300 and MAW-1350 samples.

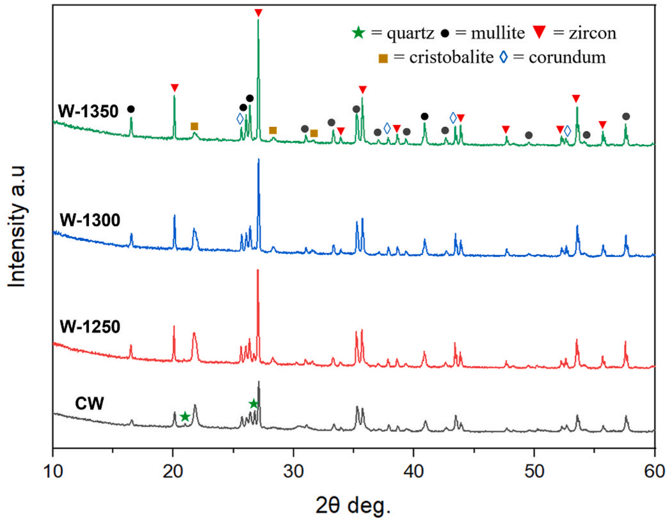

Fig. 1. XRD patterns of the W, W-1250, W-1300, and W-1350 samples. (★ = quartz, ● = mullite, ▼ = zircon, ■ = cristobalite, and ◊ = corundum).

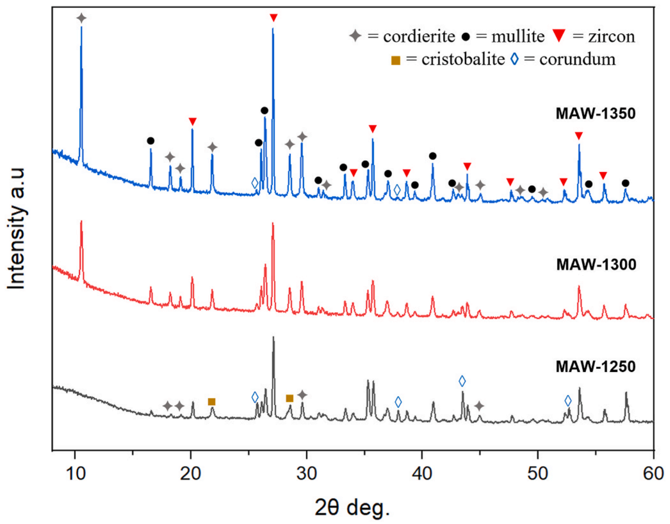

Fig. 2. XRD patterns of the MAW-1250, MAW-1300, and MAW-1350 samples. (✦ = cordierite, ● = mullite, ▼ = zircon, ■ = cristobalite, and ◊ = corundum).

The bulk density of ceramic composites produced from ICSW without additives exhibits a distinct trend with increasing sintering temperature, as shown in Fig. 3a. Specifically, the bulk densities of W-1250, W-1300, and W-1350 ceramic composites are 1.77, 1.74, and 1.80 g/cm^3, respectively. XRD analysis confirms the presence of quartz in the ICSW. Quartz undergoes phase transformations upon heating, transitioning from α-quartz to β-quartz at 573 °C, followed by β-quartz to tridymite at 870 °C, and ultimately forming cristobalite at 1470 °C. However, the presence of impurities can significantly lower the temperature at which cristobalite forms, sometimes below 1000 °C [45]. Importantly, cristobalite has a lower density than quartz, which can lead to the development of microcracks during the quartz-to-cristobalite phase transition, resulting in decreased density values.

XRD results show a gradual decrease in the intensity of quartz peaks in the ICSW as sintering temperature increases. This decrease in density, from 1.77 g/cm^3 for W-1250 to 1.74 g/cm^3 for W-1300, can be attributed to the phase changes occurring during the firing process. Subsequently, the increase from 1.74 g/cm^3 to 1.80 g/cm^3 is linked to improved densification and the formation of mullite within the silica and alumina components of the ICSW. Nevertheless, it is essential to emphasize that the overall densification of these samples remained relatively low. While there is a slight reduction in apparent porosity with increasing sintering temperature, ranging from 39.84% to 41.10%, linear shrinkage increases from 0.9% to 2.1%. The morphological features of the samples, which align with the apparent porosity results and are characterized by a porous microstructure, are presented and discussed in the supporting information.

Fig. 3b illustrates the impact of firing temperature on the flexural strength of W-1250, W-1300, and W-1350 composites. Notably, the flexural strength exhibits a modest increase with higher sintering temperatures, albeit with a relatively low rate of improvement. Indeed, the flexural strength of these samples falls within a narrow range of 8.35–8.86 MPa.

In contrast, Fig. 3d highlights a substantial contrast in flexural strength between the cordierite/mullite/zircon composites and the ceramic composites produced from ICSW without any additives. Remarkably, the MAW-1350 sample exhibited a nearly six-fold higher flexural strength compared to W-1350. This remarkable enhancement can be attributed to the development of an interlocking structure of mullite whiskers and the reduction of silica phases.

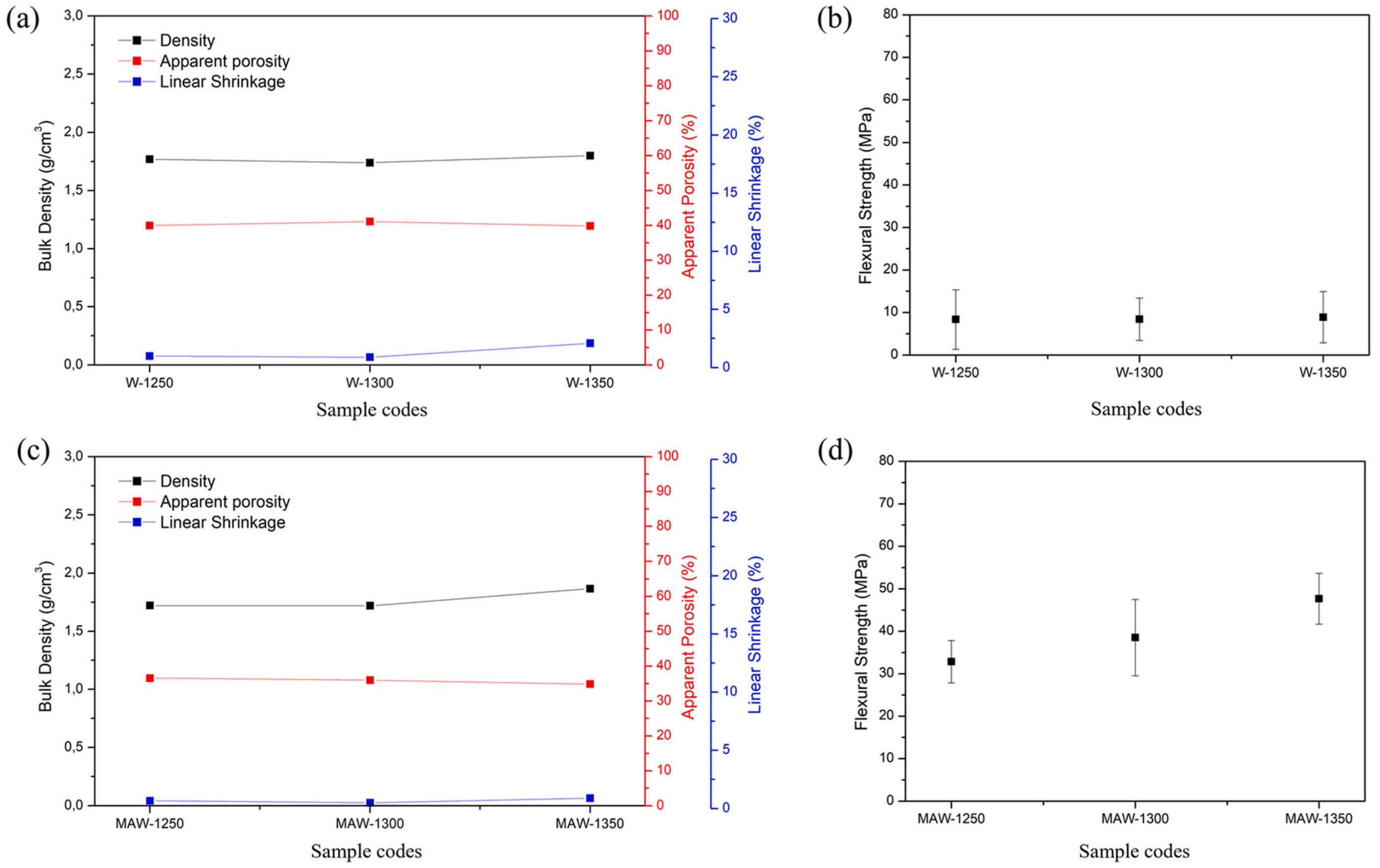

Fig. 3. Physicochemical properties of the W and MAW-series of ceramic composites.

As the porosity of the shielding material increases, the likelihood of radiation interacting with the shielding material's atoms decreases. Nevertheless, insufficient densification of the both W and MAW-series of ceramic composites are evident and their apparent porosities range between 34 and 36 vol% due to the slow diffusion process during solid-state sintering. Therefore, the effect of Y_2O_3 addition on composites' properties including degree of densification and radiation shielding properties is also investigated.

The XRD patterns of MAW-1350 and 1–10 wt% Y_2O_3-added ceramic composites synthesized at 1350 °C are presented in Fig. 4a. All specimens are identified as cordierite-zircon-mullite composites. Notably, the sharp peak at $2\theta = 10.4°$, corresponding to the cordierite phase's (100) plane, initially increases with Y_2O_3 addition, reaching its maximum with the 3 wt% Y_2O_3 additive content. However, beyond this point, the intensity starts to decline and nearly disappears for the MAW-1350-Y10 sample. Conversely, the intensity of the peak at $2\theta = 28.5°$, associated with the (222) plane, shows a significant increase, particularly when the Y_2O_3 content reaches beyond 7 wt%. Consequently, it can be concluded that the addition of Y_2O_3 influences the crystal structure, orientation, and growth behavior of cordierite crystals. Considering the known property that Y_2O_3 addition promotes the formation of liquid phases [46]. Therefore, it is plausible that the observed changes in peak intensities are associated with alterations in the dissolution, migration, and reprecipitation of Mg^{2+}, Al^{3+}, and Si^{4+} within the liquid media. These processes may contribute to the modification of crystal growth kinetics and morphology, ultimately influencing the XRD patterns observed in the synthesized composites.

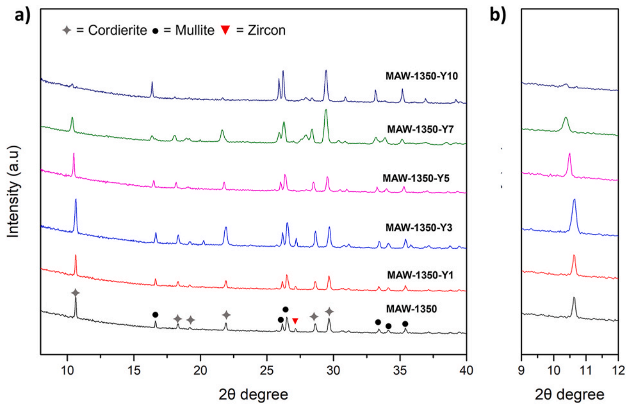

Fig. 4. XRD patterns of the MAW-1350 and MAW-Y1-10 samples. (✦ = cordierite, ● = mullite, ▼ = zircon, and ■ = alumina).

The crystal structure of cordierite consists of six-membered rings composed of alternating aluminum and silicon tetrahedra, forming a framework structure. It is noteworthy that cordierite exhibits two polymorphs: a high symmetry hexagonal phase (*P6/mcc* No. 192) and low symmetry orthorhombic phase (*Cccm* No. 66), which typically coexisting. In the high symmetry hexagonal phase, $Si_4Al_2O_{18}$ six-membered tetrahedron rings contain ordered SiO_4 and AlO_4 tetrahedra. Contrarily, in the low symmetry polymorph, the hexagonal rings undergo distortion, resulting in an orthorhombic crystal lattice [47].

Remarkably, the addition of 7–10 wt% Y_2O_3 results in increased peak splitting, suggesting a greater presence of the orthorhombic phase. This change is likely associated with reduced Si/Al ordering in the $Si_4Al_2O_{18}$ six-membered rings due to the introduction of Y_2O_3. Additionally, the peak at $2\theta = 10.4°$ shifts toward lower angles with increasing Y_2O_3 addition, as observed in Fig. 4b. This shift indicates the doping of Y^{3+} ions into the cordierite lattice, leading to increased unit cell volumes since the size of Y^{3+} is considerably larger than Al^{3+}, Si^{2+}, and Mg^{2+}.

Considering the incorporation of Y^{3+} in the cordierite lattice, one possibility is the replacement of Mg^{2+} ions in octahedral sites, as the size of Y^{3+} is more compatible with these sites. Additionally, it is probable that Y^{3+} can enter the hexagonal channels in the $Si_4Al_2O_{18}$ six-membered rings—a phenomenon observed with other large cations [48,49]. In this case, the Al^{3+}/Si^{4+} ratio in tetrahedra increases with the rising Y^{3+} content due to charge balance. This change leads to lattice expansion and distortion of corresponding polyhedra due to the relatively larger length of Al–O bonds compared to Si–O bonds. This lattice variation, coupled with the reduction in Si/Al ordering in the six-membered rings, is likely the reason for the observed reduction in crystal symmetry in cordierite.

The addition of Y_2O_3 enhances bulk density and reduces apparent porosity by generating a vitreous phase. This vitreous phase promotes viscous flow sintering and particle rearrangement, resulting in the closure of open pores. In Y_2O_3-added composites, bulk density progressively increases with higher Y_2O_3 content, while apparent porosity decreases (as depicted in Fig. S3). For example, the addition of 10 wt% Y_2O_3 increases bulk density from 1.86 g/cm^3 in MAW-1350 to 2.17 g/cm^3. This substantial improvement in bulk density is anticipated to enhance the radiation shielding capability of the composites.

The mass attenuation coefficient (MAC) is a critical parameter describing a material's ability to attenuate or reduce the intensity of ionizing radiation. A higher MAC indicates that the material is more effective for shielding against gamma rays. MAC is a material-specific constant that depends on the elemental composition [50,51]. Therefore, the MAC values for W-1250, W-1300, and W-1350 were found to be identical across the entire photon energy range. Similarly, the MAC variations for MAW-1250, MAW-1300, and MAW-1350 with incident photon energy were also consistent (as shown in Fig. S4).

The photon energy range can be categorized into three regions based on the prevailing type of interaction. In the low-energy region, up to 0.1 MeV, attenuation decreases significantly. The primary interaction mechanism within this range is photoelectric absorption, and it's highly sensitive to the atomic numbers of the elements in shielding materials. Elements with higher atomic numbers provide more electrons for photon interaction, increasing the likelihood of photon absorption [52–56]. While the MAC variations of the W- and MAW-series samples are quite similar, the W-series exhibits slightly greater attenuation compared to the MAW series in the region dominated by photoelectric absorption. This distinction arises because the W-series is directly fabricated from ICSW, whereas MgO with a lower molar weight is added to investment-casting shell waste to produce cordierite/mullite/zircon composites.

On the other hand, the atomic mass of Y is higher than that of Mg, Al, and Si. Consequently, in the low energy region up to 0.1 MeV, the mass attenuation coefficient values demonstrate a direct relation with the Y_2O_3 content and follow the order of MAW-1350-Y10 > MAW-1350-Y7 > MAW-1350-Y5 >MAW-1350-Y3 > MAW-1350-Y1 > MAW-1350 (as depicted in Fig. 5).

Compton scattering becomes the predominant attenuation mechanism in moderate photon energy regions, typically ranging from 0.1 MeV up to several MeV [57]. While not as pronounced as in the low-energy zone, attenuation continues to decrease with increasing photon energy within this intermediate energy range, ranging from 0.1 MeV to 3 MeV. Importantly, Compton scattering is relatively insensitive to the atomic number of constituent elements. Therefore, the disparities between the mass attenuation coefficient values of the composites are markedly reduced (Inset Fig. 5a). In the high-energy region, specifically above 3 MeV, the mass attenuation coefficient of the composites exhibits a slight increase due to the pair production phenomenon. Beyond this point, as incoming photon energy further rises, the coefficient stabilizes, remaining nearly constant.

Furthermore, the gamma shielding parameters of W-1350, MAW-1350, and MAW-1350-Y10 (as detailed in Table S2) were experimentally evaluated and compared with their theoretically calculated counterparts. Fig. S5 illustrates the reasonable agreement between experimentally measured MAC values and their theoretical counterparts.

The linear attenuation coefficient (LAC) refers to the fraction of an X-ray or gamma-ray beam that is either absorbed or scattered per unit thickness of the shielding material [58]. This coefficient is influenced by the atomic weights of the elements within the shielding materials and their densities. Generally, materials with higher density tend to be more effective at attenuating gamma rays because there are more atoms or particles within a given thickness to interact with and absorb the radiation. The linear attenuation coefficient (LAC) of the samples shows a direct relationship with both the sintering temperature and the Y_2O_3 additive content. As the sintering temperature and Y_2O_3 additive content increase, the LAC also increases, indicating that the ability of the samples to attenuate gamma radiation becomes enhanced (Fig. 5b).

The mean free path (MFP) represents the average distance a gamma ray can travel within the shielding material before interacting. In the low-energy region, all composites exhibit low MFP values, and these values increase as the photon energy rises. This trend indicates that the shielding effectiveness of the composites diminishes as photon energy increases (Fig. 6a–c). MFP values for all composites remain almost zero up to photon energies of roughly 30 keV, indicating that photons with energies less than 30 keV cannot penetrate deep into the fabricated ceramics. Nevertheless, beyond 100 keV MFP values steadily increases

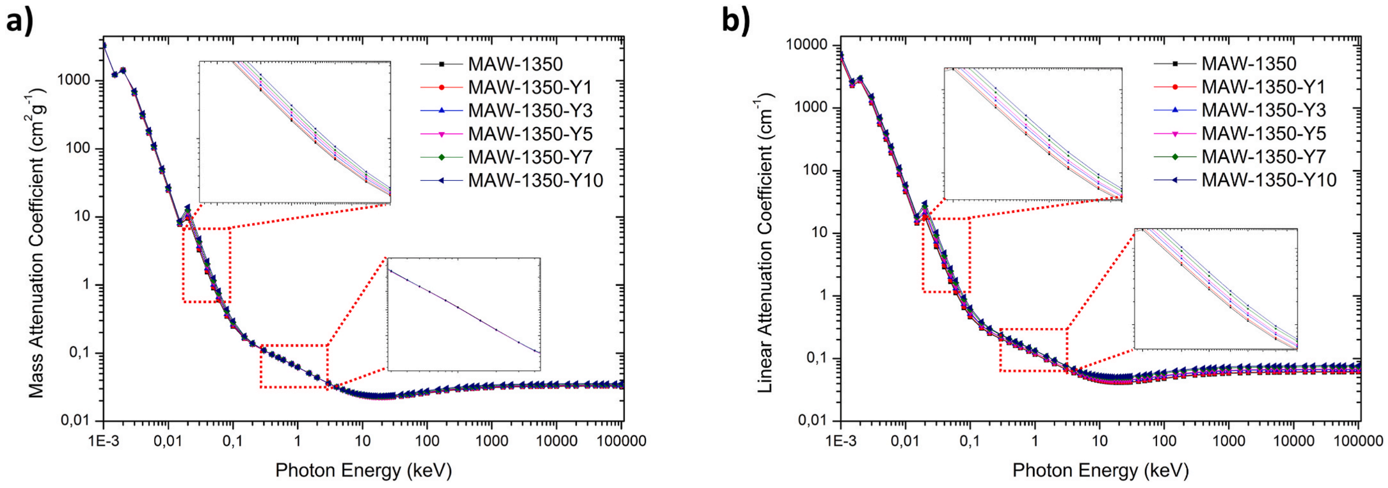

Fig. 5. The relative variations of mass attenuation coefficient (a) and linear attenuation coefficient (b) for MAW-Y1-10.

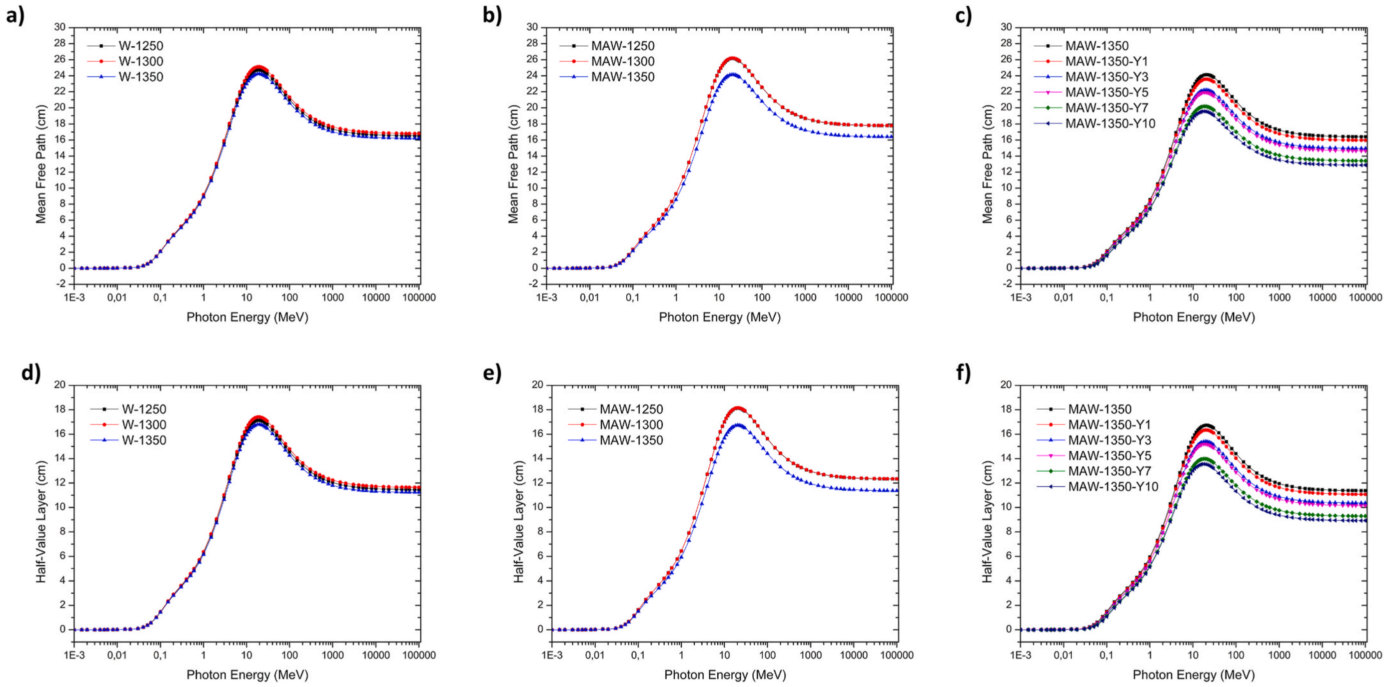

Fig. 6. The variations of mean free path and half-value layer of ceramic composites with photon energy.

for all composites. Maxiumum MFP values are observed at around 20 MeV photon energy. The maximum MFP values for W1250, W-1300, and W-1350 are 24.71, 25.12, and 24.23 cm, respectively. Similarly, the maximum MFP values for MAW-1250, MAW-1300, and MAW-1350 are 26.15, 26.21, and 24.14 cm. Notably, the MFP of MAW-1350 decreases by about 25% with the addition of 10 wt% Y_2O_3. MAW-1350-Y10, the densest material among all composites, exhibits the smallest MFP values (18 cm at 20 MeV). This occurs because photons encounter more collisions while traveling through the pores of this dense material.

Half-value layers (HVL) represent the required material thickness to reduce the incoming photon beam intensity by 50% [59,60]. The trend in HVL closely parallels that of MFP. HVL values also exhibit a strong correlation with both sintering temperature and Y_2O_3 additive content (Fig. 6d–f). Notably, MAW-1350-Y10 stands out with the smallest HVL values across the entire photon energy range. This is attributed to its higher density and yttrium content.

Fig. 7 illustrates the effective atomic numbers (Z_{eff}) for the studied composites at different energies. It can be seen that the Z_{eff} values correlate well with the Y_2O_3 content. At any specific energy, MAW-1350-Y10 demonstrates the highest Z_{eff}, while MAW-1350 has the lowest. Nonetheless, Z_{eff} values of the all composites follow the similar trend.

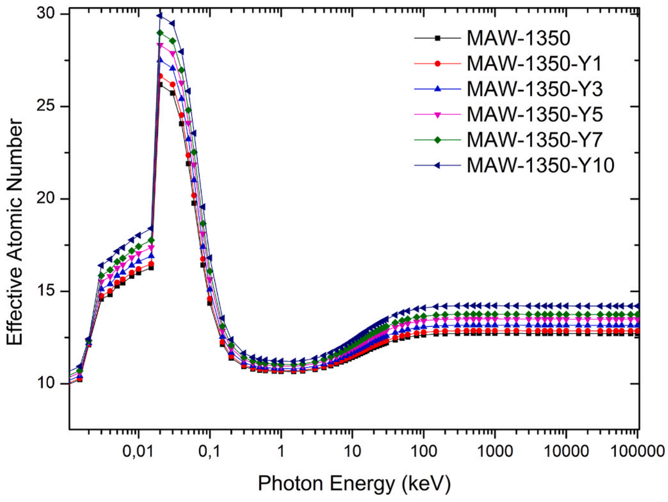

Fig. 7. Effective atomic number for MAW-Y1-10.

In the low-energy region, Z_{eff} values increase significantly with rising photon energy, with the highest Z_{eff} values observed in this region, where photoelectric absorption is the dominant interaction mechanism. The maximum Z_{eff} values are obtained at 0.02 MeV, with values of 29.91, 28.98, 28.32, 27.51, 26.65, and 26.18 for MAW-1350-Y10, MAW-1350-Y7, MAW-1350-Y5, MAW-1350-Y3, MAW-1350-Y1, and MAW-1350, respectively.

In the subsequent energy region, where Compton scattering governs the interaction, a rapid decline in Z_{eff} values is observed until Z_{eff} values reach their lowest points between 0.5 and 2 MeV. Afterward, Z_{eff} values exhibit a mild increase with increasing energy, driven by the pair production effect.

The neutron shielding capabilities of ceramic samples were assessed by calculating their fast neutron removal cross-sections (FNRCS). The FNRCS value of a material depends on the total neutron absorption cross-sections of the elements within the absorbent material and the material's density. Notably, among the W-series of samples, W-1350 exhibits the highest FNRCS value, while W-1300 displays the lowest, a trend that aligns well with their respective densities (as shown in Fig. S6). A similar trend is also observed in the MAW series of samples.

Furthermore, the FNRCS value of MAW-1350 surpasses that of W-1350, indicating that creating cordierite-based composites from investment casting shells is advantageous for achieving enhanced neutron attenuation performance. Moreover, the addition of Y_2O_3 further enhances the material's neutron shielding ability. This can be explained by two reasons: first, the likelihood of an interaction between the neutrons and the atoms of the attenuator increases with decreasing apparent porosity. Secondly, the neutron cross-section of Y (1.28) is considerably higher than that of Mg (0.063), Al (0.233), and Si (0.166). Therefore, Y has a higher probability of interacting with incident neutrons. MAW-1350-Y10 has the highest fast FNRCS among the all fabricated ceramic composites with $\Sigma R = 0.069$ cm^{-1} and its FNRCS is comparable to some commonly used neutron shielding materials such as graphite ($\Sigma R =$

0.077 cm^{-1}) and paraffin ($\Sigma R = 0.0773\ cm^{-1}$), and concrete ($\Sigma R = 0.094\ cm^{-1}$) [61,62].

4. Conclusions

In this study, eco-friendly cordierite-mullite-zircon composites were fabricated from investment casting shell waste, alumina, and magnesia as raw materials. The influence of sintering temperature and Y_2O_3 addition on the composites' structural, physical, and radiation shielding properties were investigated. From our study, the following conclusions can be drawn.

1 XRD analysis revealed that the investment-casting shell waste comprises silica, mullite, alumina, and zircon. Thereby, cordierite/mullite/zircon ceramic composites could be obtained by firing appropriate mixtures of investment-casting shell waste, alumina, and magnesia. All the free silica in the investment casting shell waste was consumed to yield cordierite for samples fired at 1300 °C and 1350 °C for 3 h.

2 Flexural strength improved with increasing sintering temperature; it reached 47.69 Mpa for the sample sintered at 1350 °C. The flexural strength of MAW-1350 was almost 6 times higher than the ceramic composite fabricated directly from investment cast shell waste at the same sintering temperature. The enhanced mechanical properties of the cordierite/mullite/zircon composite were attributed to the removal of silica phases, the formation of the interlocking structure of elongated mullites, and the enhanced densification behavior of the composites with increasing sintering temperature.

3 The density of the composites increased with the rising concentration of Y_2O_3. Meanwhile, the apparent porosity is reduced. These outcomes attained enhanced radiation shielding ability for the composites. Indeed, the mass attenuation coefficient, linear attenuation coefficient, and Z_{eff} increased with increasing Y_2O_3 addition. Contrarily, the mean free path and half-value layer of the composites decreased with increased Y_2O_3 concentration. Nevertheless, Y_2O_3 addition had more influence in the low-energy region where photoelectric absorption is the governing effect. Besides, composites are more effective in radiation shielding in the low-energy region and their shielding ability became worse at high photon energies (>1 MeV). Moreover, theoretical and experimental studies showed good agreement with each other.

Consequently, the results of this work demonstrate the possibility of utilizing investment-casting shell waste in producing light and non-toxic radiation shielding materials.

Declaration of competing interest

The authors declare that they have no known competing financial interests or personal relationships that could have appeared to influence the work reported in this paper.

Acknowledgments

The authors would like to express their sincere gratitude to Asst. Prof. Dr. Yaşar Karabul for his help with gamma-ray shielding experiments.

Appendix A. Supplementary data

Supplementary data to this article can be found online at https://doi.org/10.1016/j.net.2024.02.038.

References

[1] P. Kalita, S. Ghosh, G. Sattonnay, U.B. Singh, V. Grover, R. Shukla, S. Amirthapandian, R. Meena, A.K. Tyagi, D.K. Avasthi, Role of temperature in the radiation stability of yttria stabilized zirconia under swift heavy ion irradiation: a study from the perspective of nuclear reactor applications, J. Appl. Phys. 122 (2017) 025902, https://doi.org/10.1063/1.4993177.

[2] A. Aboalatta, J. Asad, M. Humaid, H. Musleh, S. Shaat, K. Ramadan, M.I. Sayyed, Y. Alajerami, N. Aldahoudi, Experimental investigation of zinc sodium borate glass systems containing barium oxide for gamma radiation shielding applications, Nucl. Eng. Technol. 53 (2021) 3058–3067, https://doi.org/10.1016/j.net.2021.04.002.

[3] F. Akman, H. Ogul, I. Ozkan, M.R. Kaçal, O. Agar, H. Polat, K. Dilsiz, Study on gamma radiation attenuation and non-ionizing shielding effectiveness of niobium-reinforced novel polymer composite, Nucl. Eng. Technol. 54 (2022) 283–292, https://doi.org/10.1016/j.net.2021.07.006.

[4] Y. Al-Hadeethi, M.I. Sayyed, Correlation between the concentration of TeO2 and the radiation shielding properties in the TeO2–MoO3–V2O5 glass system, Nucl. Eng. Technol. 55 (2023) 1218–1224, https://doi.org/10.1016/j.net.2022.12.014.

[5] I.G. Alhindawy, H. Gamal, A. Almuqrin, M.I. Sayyed, K.A. Mahmoud, Impacts of the calcination temperature on the structural and radiation shielding properties of the NASICON compound synthesized from zircon minerals, Nucl. Eng. Technol. 55 (2023) 1885–1891, https://doi.org/10.1016/j.net.2023.02.014.

[6] S. Arivazhagan, K.A. Naseer, K.A. Mahmoud, S.A. Bassam, P.N. Naseef Mohammed, N.K. Libeesh, A.S. Sachana, M.I. Sayyed, M.S. Alqahtani, E. El Shiekh, M. U. Khandaker, The radiation shielding competence and imaging spectroscopic based studies of Iron ore region of Kozhikode district, Kerala, Nucl. Eng. Technol. 55 (2023) 2380–2387, https://doi.org/10.1016/j.net.2023.03.038.

[7] C. Avcıoğlu, S. Avcıoğlu, Transition metal borides for all-in-one radiation shielding, Materials 16 (2023) 6496, https://doi.org/10.3390/ma16196496.

[8] S. Avcıoğlu, F. Kaya, C. Kaya, Morphological evolution of boron carbide particles: sol-gel synthesis of nano/micro B4C fibers, Ceram. Int. 47 (2021) 26651–26667, https://doi.org/10.1016/j.ceramint.2021.06.073.

[9] N. Baumann, K.M. Diaz, K. Simmons-Potter, B.G. Potter, J. Bucay, Particle loading as a design parameter for composite radiation shielding, Nucl. Eng. Technol. 54 (2022) 3855–3863, https://doi.org/10.1016/j.net.2022.05.029.

[10] E. Beyazay, Y. Karabul, S.E. Korkut, M. Kılıç, Z.G. Özdemir, Multifunctional PCz/BaO nanocomposites: ionizing radiation shielding ability and enhanced electric conductivity, Prog. Nucl. Energy 155 (2023) 104521, https://doi.org/10.1016/j.pnucene.2022.104521.

[11] Ö. Can, E. Eren Belgin, G.A. Aycik, Effect of different tungsten compound reinforcements on the electromagnetic radiation shielding properties of neopentyl glycol polyester, Nucl. Eng. Technol. 53 (2021) 1642–1651, https://doi.org/10.1016/j.net.2020.11.006.

[12] B.M. Chandrika, H.C.S. Manjunatha, K.N. Sridhar, M.R. Ambika, L. Seenappa, S. Manjunatha, R. Munirathnam, A.C. Lourduraj, Synthesis, physical, optical and radiation shielding properties of Barium-Bismuth Oxide Borate-A novel nanomaterial, Nucl. Eng. Technol. 55 (2023) 1783–1790, https://doi.org/10.1016/j.net.2023.01.012.

[13] M.S. Eid, I.I. Bondouk, H.M. Saleh, K.M. Omar, M.I. Sayyed, A.M. El-Khatib, M. Elsafi, Implementation of waste silicate glass into composition of ordinary cement for radiation shielding applications, Nucl. Eng. Technol. 54 (2022) 1456–1463, https://doi.org/10.1016/j.net.2021.10.007.

[14] M.Y. Hanfi, A.K. Sakr, A.M. Ismail, B.M. Atia, M.S. Alqahtani, K.A. Mahmoud, Physical characterization and radiation shielding features of B2O3As2O3 glass ceramic, Nucl. Eng. Technol. 55 (2023) 278–284, https://doi.org/10.1016/j.net.2022.09.006.

[15] G. Hu, H. Hu, Q. Yang, B. Yu, W. Sun, Study on the design and experimental verification of multilayer radiation shield against mixed neutrons and γ-rays, Nucl. Eng. Technol. 52 (2020) 178–184, https://doi.org/10.1016/j.net.2019.07.016.

[16] S.A. Issa, A.M. Ali, H.O. Tekin, Y.B. Saddeek, A. Al-Hajry, H. Algarni, G. Susoy, Enhancement of nuclear radiation shielding and mechanical properties of YBiBO3 glasses using La2O3, Nucl. Eng. Technol. 52 (2020) 1297–1303, https://doi.org/10.1016/j.net.2019.11.017.

[17] T.H. Khazaalah, I.S. Mustafa, M.I. Sayyed, Radiation parameterizations and optical characterizations for glass shielding composed of SLS waste glass and lead-free materials, Nucl. Eng. Technol. 54 (2022) 4708–4714, https://doi.org/10.1016/j.net.2022.08.009.

[18] L.F. Pires, Radiation shielding properties of weathered soils: influence of the chemical composition and granulometric fractions, Nucl. Eng. Technol. 54 (2022) 3470–3477, https://doi.org/10.1016/j.net.2022.04.002.

[19] B.C. Reddy, H.C. Manjunatha, Y.S. Vidya, K.N. Sridhar, U.M. Pasha, L. Seenappa, B. Sadashivamurthy, N. Dhananjaya, K.V. Sathish, P.D. Gupta, X-ray/gamma ray radiation shielding properties of α-Bi2O3 synthesized by low temperature solution combustion method, Nucl. Eng. Technol. 54 (2022) 1062–1070, https://doi.org/10.1016/j.net.2021.09.023.

[20] V.G. Rudychev, N.A. Azarenkov, I.O. Girka, Y.V. Rudychev, Optimization of radiation shields made of Fe and Pb for the spent nuclear fuel transport casks, Nucl. Eng. Technol. 55 (2023) 690–695, https://doi.org/10.1016/j.net.2022.10.002.

[21] K.V. Sathish, K.N. Sridhar, L. Seenappa, H.C. Manjunatha, Y.S. Vidya, B. Chinnappa Reddy, S. Manjunatha, A.N. Santhosh, R. Munirathnam, A.C. Raj, P.S. Damodara Gupta, B.M. Sankarshan, X-ray/gamma radiation shielding properties of Aluminium-Barium Zinc Oxide nanoparticles synthesized via low temperature solution combustion method, Nucl. Eng. Technol. 55 (2023) 1519–1526, https://doi.org/10.1016/j.net.2023.02.001.

[22] P. Vani, G. Vinitha, M.I. Sayyed, M.M. AlShammari, N. Manikandan, Effect of rare earth dopants on the radiation shielding properties of barium tellurite glasses,

Nucl. Eng. Technol. 53 (2021) 4106–4113, https://doi.org/10.1016/j.net.2021.06.009.

[23] M. Zaid, K.A. Matori, H. Sidek, I.R. Ibrahim, Bismuth modified gamma radiation shielding properties of titanium vanadium sodium tellurite glasses as a potent transparent radiation-resistant glass applications, Nucl. Eng. Technol. 53 (2021) 1323–1330, https://doi.org/10.1016/j.net.2020.10.006.

[24] M.A. Zakaria, Abdul Razak, Mohammad Khairul Azhar, M.Z. Adenan, M.Z. Ahmad, S.M. Tajudin, D.O. Samson, M.Z. Abdul Aziz, Radiation attenuation and elemental composition of locally available ceramic tiles as potential radiation shielding materials for diagnostic X-ray rooms, Nucl. Eng. Technol. (2023), https://doi.org/10.1016/j.net.2023.10.001.

[25] Ü. Alver, S.U. Duran, M.B. Demirköz, B. Muçogllava, M. Aslan, K. Çava, F. Özkalaycı, O. Dindar, Ulexite/HDPE-Bi2O3/HDPE layered composites for neutron and gamma radiation shielding, Appl. Radiat. Isot. 200 (2023) 110940, https://doi.org/10.1016/j.apradiso.2023.110940.

[26] M. Özcan, C. Kaya, F. Kaya, Cosmic radiation shielding property of boron reinforced continuous fiber nanocomposites produced by electrospinning, Discover Nano 18 (2023) 152, https://doi.org/10.1186/s11671-023-03940-3.

[27] Y. Kobayashi, M. Katayama, M. Kato, S. Kuramochi, Effect of microstructure on the thermal expansion coefficient of sintered cordierite prepared from sol mixtures, J. Am. Ceram. Soc. 96 (2013) 1863–1868, https://doi.org/10.1111/jace.12195.

[28] F.C. Oliveira, V. Livramento, F. Delmas, Novel mullite-based ceramics manufactured from inorganic wastes, J. Mater. Process. Technol. 196 (2008) 101–108, https://doi.org/10.1016/j.jmatprotec.2007.05.011.

[29] D. Kuscer, I. Bantan, M. Hrovat, B. Malič, The microstructure, coefficient of thermal expansion and flexural strength of cordierite ceramics prepared from alumina with different particle sizes, J. Eur. Ceram. Soc. 37 (2017) 739–746, https://doi.org/10.1016/j.jeurceramsoc.2016.08.032.

[30] A. Chowdhury, S. Maitra, H.S. Das, A. Sen, G.K. Samanta, P. Datta, Synthesis, properties and applications of cordierite ceramics, Part 2 56 (2007) 98–102.

[31] Z. Lei, H. Gao, X. Chang, L. Zhang, X. Wen, Y. Wang, An application of green surfactant synergistically metal supported cordierite catalyst in denitration of Selective Catalytic Oxidation, J. Clean. Prod. 249 (2020) 119307, https://doi.org/10.1016/j.jclepro.2019.119307.

[32] L.D. Zobina, G.D. Semchenko, R.A. Tarnopol'skaya, Y.G. Belik, F.Y. Kharitonov, V. P. Rudnitskaya, Synthesis of cordierite from natural materials in the presence of Al2O3-containing components, Refractories 28 (1987) 82–84, https://doi.org/10.1007/BF01386734.

[33] V.N. Antsiferov, S.E. Porozova, S.N. Peshcherenko, Effect of the raw materials on the properties of cordierite ceramics, Refract. Ind. Ceram. 38 (1997) 388–391, https://doi.org/10.1007/BF02767900.

[34] E.P. de Almeida, I.P. de Brito, H.C. Ferreira, H.d.L. Lira, L.N. de Lima Santana, G. de Araújo Neves, Cordierite obtained from compositions containing kaolin waste, talc and magnesium oxide, Ceram. Int. 44 (2018) 1719–1725, https://doi.org/10.1016/j.ceramint.2017.10.102.

[35] H. Hajjou, L. Saâdi, M. Waqif, Synthesis of cordierite using industrial waste fly ash, Arabian J. Geosci. 10 (2017) 1–9, https://doi.org/10.1007/s12517-017-3156-0.

[36] R.M. Khattab, H.H. Abo-Almaged, N.A. Ajiba, H.A. Badr, A.A. Gaber, M.A. Taha, H. Sadek, Sintering, physicomechanical, thermal expansion and microstructure properties of cordierite ceramics based on utilizing silica fume waste, Mater. Chem. Phys. 270 (2021) 124829, https://doi.org/10.1016/j.matchemphys.2021.124829.

[37] S. Wang, H. Wang, Z. Chen, R. Ji, L. Liu, X. Wang, Fabrication and characterization of porous cordierite ceramics prepared from fly ash and natural minerals, Ceram. Int. 45 (2019) 18306–18314, https://doi.org/10.1016/j.ceramint.2019.06.043.

[38] M.I. Sayyed, M.A. Abdo, H.E. Ali, M.S. Sadeq, Effect of Y2O3 on the structural, optical and radiation shielding properties of transparent Na-rich borate glass with diluted and fixed Fe2O3, Ceram. Int. 48 (2022) 24310–24318, https://doi.org/10.1016/j.ceramint.2022.04.226.

[39] C. Avcıoğlu, M.F. Bekheet, R. Artır, Radiation shielding and mechanical properties of mullite-zirconia composites fabricated from investment-casting shell waste, J. Mater. Res. Technol. 24 (2023) 5883–5895, https://doi.org/10.1016/j.jmrt.2023.04.190.

[40] M. Bozkurt, N. Şahin, Y. Karabul, M. Kılıç, Z.G. Özdemir, Radiation shielding performances of Na2SiO3 based low-cost micro and nano composites for diagnostic imaging, Prog. Nucl. Energy 143 (2022) 104058, https://doi.org/10.1016/j.pnucene.2021.104058.

[41] N. Şahin, M. Bozkurt, Y. Karabul, M. Kılıç, Z.G. Özdemir, Low cost radiation shielding material for low energy radiation applications: epoxy/Yahyali Stone composites, Prog. Nucl. Energy 135 (2021) 103703, https://doi.org/10.1016/j.pnucene.2021.103703.

[42] E. Beyazay, Y. Karabul, S.E. Korkut, M. Kılıç, Z.G. Özdemir, Multifunctional PCz/BaO nanocomposites: ionizing radiation shielding ability and enhanced electric conductivity, Prog. Nucl. Energy 155 (2023) 104521, https://doi.org/10.1016/j.pnucene.2022.104521.

[43] F.C. Hila, A. Asuncion-Astronomo, C.A.M. Dingle, J.F.M. Jecong, A.M.V. Javier-Hila, M.B.Z. Gili, C.V. Balderas, G.E.P. Lopez, N.R.D. Guillermo, A.V. Amorsolo, EpiXS: a Windows-based program for photon attenuation, dosimetry and shielding based on EPICS2017 (ENDF/B-VIII) and EPDL97 (ENDF/B-VI.8), Radiat. Phys. Chem. 182 (2021) 109331, https://doi.org/10.1016/j.radphyschem.2020.109331.

[44] E. Şakar, Ö.F. Özpolat, B. Alım, M.I. Sayyed, M. Kurudirek, Phy-X/PSD: development of a user friendly online software for calculation of parameters relevant to radiation shielding and dosimetry, Radiat. Phys. Chem. 166 (2020) 108496, https://doi.org/10.1016/j.radphyschem.2019.108496.

[45] S. Zhang, S. Tie, F. Zhang, Cristobalite formation from the thermal treatment of amorphous silica fume recovered from the metallurgical silicon industry, Micro & Nano Lett. 13 (2018) 1465–1468, https://doi.org/10.1049/mnl.2018.5167.

[46] C. Hu, W. Xiang, P. Chen, Q. Li, R. Xiang, L. Zhou, Influence of Y2O3 on densification, flexural strength and heat shock resistance of cordierite-based composite ceramics, Ceram. Int. 48 (2022) 74–81, https://doi.org/10.1016/j.ceramint.2021.09.082.

[47] H. Ohsato, J.-S. Kim, C.-I. Cheon, I. Kagomiya, Millimeter-wave dielectrics of indialite/cordierite glass ceramics: estimating Si/Al ordering by volume and covalency of Si/Al octahedron, J. Ceram. Soc. Japan 121 (2013) 649–654, https://doi.org/10.2109/jcersj2.121.649.

[48] J. Zhou, Z. Xia, M. Chen, M.S. Molokeev, Q. Liu, New insight into phase formation of MxMg2Al(4+x)Si(5-x)O18:Eu2+ solid solution phosphors and its luminescence properties, Sci. Rep. 5 (2015) 12149, https://doi.org/10.1038/srep12149.

[49] D. Wei, H.J. Seo, Determination of phase-formation of (Mg 1−x Mn x) 2 Al 4 Si 5 O 18 (x = 0–1) cordierite solid-solutions via crystallographic sites and luminescence dynamics of Mn 2+ centers, J. Mater. Chem. C 8 (2020) 7899–7907, https://doi.org/10.1039/D0TC01143F.

[50] M. Çağlar, Y. Karabul, M. Kılıç, Z.G. Özdemir, O. İçelli, Na2Si3O7/Ag micro and nano-structured glassy composites: the experimental and MCNP simulation surveys of their radiation shielding performances, Prog. Nucl. Energy 139 (2021) 103855, https://doi.org/10.1016/j.pnucene.2021.103855.

[51] C. Avcıoğlu, R. Artır, Utilization of investment casting shell waste in the production of cordierite-mullite-zircon composites for radiation shielding: the influence of La2O3 additive, Ceram. Int. 50 (2024) 4581–4588, https://doi.org/10.1016/j.ceramint.2023.11.199.

[52] S. Avcıoğlu, M. Buldu, F. Kaya, C. Kaya, Synthesis of nuclear-grade nano-sized boron carbide powders and its application in LDPE matrix composites for neutron shielding, Compos. Mater. Manuf. Prop. Appl. (2021) 543–579, https://doi.org/10.1016/B978-0-12-820512-9.00019-8.

[53] S. Avcıoğlu, M. Buldu, F. Kaya, C.B. Üstündağ, E. Kam, Y.Z. Menceloğlu, H. Y. Kaptan, C. Kaya, Processing and properties of boron carbide (B4C) reinforced LDPE composites for radiation shielding, Ceram. Int. 46 (2020) 343–352, https://doi.org/10.1016/j.ceramint.2019.08.268.

[54] Z. Lei, H. Gao, X. Chang, L. Zhang, X. Wen, Y. Wang, An application of green surfactant synergistically metal supported cordierite catalyst in denitration of Selective Catalytic Oxidation, J. Clean. Prod. 249 (2020) 119307, https://doi.org/10.1016/j.jclepro.2019.119307.

[55] M. Alwaeli, Investigation of gamma radiation shielding and compressive strength properties of concrete containing scale and granulated lead-zinc slag wastes, J. Clean. Prod. 166 (2017) 157–162, https://doi.org/10.1016/j.jclepro.2017.07.203.

[56] N. Saca, L. Radu, V. Fugaru, M. Gheorghe, I. Petre, Composite materials with primary lead slag content: application in gamma radiation shielding and waste encapsulation fields, J. Clean. Prod. 179 (2018) 255–265, https://doi.org/10.1016/j.jclepro.2018.01.045.

[57] T. Demirbay, M. Çağlar, Y. Karabul, M. Kılıç, O. İçelli, Z. Güven Özdemir, Availability of water glass/Bi 2 O 3 composites in dielectric and gamma-ray screening applications, Radiat. Eff. Defect Solid 174 (2019) 419–434, https://doi.org/10.1080/10420150.2019.1596109.

[58] M.E. Mahmoud, A.M. El-Khatib, M.S. Badawi, A.R. Rashad, R.M. El-Sharkawy, A. A. Thabet, Recycled high-density polyethylene plastics added with lead oxide nanoparticles as sustainable radiation shielding materials, J. Clean. Prod. 176 (2018) 276–287, https://doi.org/10.1016/j.jclepro.2017.12.100.

[59] M. Özcan, S. Avcıoğlu, C. Kaya, F. Kaya, Boron carbide reinforced electrospun nanocomposite fiber mats for radiation shielding, Polym. Compos. (2023), https://doi.org/10.1002/pc.27387 pc.27387.

[60] S. Avcıoğlu, LDPE matrix composites reinforced with dysprosium-boron containing compounds for radiation shielding applications, J. Alloys Compd. 927 (2022) 166900, https://doi.org/10.1016/j.jallcom.2022.166900.

[61] E. Ilik, E. Kavaz, G. Kilic, S.A. Issa, H.M. Zakaly, H.O. Tekin, A closer-look on Copper(II) oxide reinforced Calcium-Borate glasses: fabrication and multiple experimental assessment on optical, structural, physical, and experimental neutron/gamma shielding properties, Ceram. Int. 48 (2022) 6780–6791, https://doi.org/10.1016/j.ceramint.2021.11.229.

[62] O.I. Sallam, A.M. Madbouly, N.L. Moussa, A. Abdel-Galil, Impact of radiation on CoO-doped borate glass: lead-free radiation shielding, Appl. Phys. A 128 (2022) 1–16, https://doi.org/10.1007/s00339-021-05190-5.